Research Article | Vol. 30, No. 5 / 28 Feb 2022 / Optics Express 7725

Optics EXPRESS

Dynamic polarization-insensitive BOTDA in direct-detection OFDM with CNN-based BFS extraction

DI QI,[1] JINGYU LI,[2] XUN GUAN,[3,4] AND CHUN-KIT CHAN[1,5]

[1] *Lightwave Communications Laboratory, Department of Information Engineering, The Chinese University of Hong Kong, Shatin, N.T., Hong Kong, China*
[2] *DSP & Speech Technology Laboratory (DSP-STL), Department of Electronic Engineering, The Chinese University of Hong Kong, Shatin, N.T., Hong Kong, China*
[3] *Centre for Optics, Photonics and Laser (COPL), Université Laval, Quebec, QC G1V 0A6, Canada*
[4] *xun.guan.1@ulaval.ca*
[5] *ckchan@ie.cuhk.edu.hk*

Abstract: We propose a dynamic polarization-insensitive Brillouin optical time domain analyzer (D/PI-BOTDA) with orthogonal frequency division multiplexing (OFDM) based on intensity-modulated direct-detection (IM-DD). A polarization-division-multiplexed (PDM) pump signal enables polarization diversity of the stimulated Brillouin scattering while a multi-frequency OFDM probe signal realizes dynamic sensing with single-shot transmission. We experimentally demonstrated distributed temperature sensing along a total 940-meter fiber with a temperature sensing coefficient of 1.2°C/MHz. The experimental results indicated a remarkable suppression of Brillouin gain fluctuation up to 4.38 times compared to the case without polarization diversity. To facilitate the Brillouin frequency shift (BFS) extraction process, we also implement a CNN-based BFS extraction method with SE-Res2Net block. The adopted algorithm achieves a higher accuracy than conventional curve fitting method, with a 10-time enhancement in the time efficiency.

1. Introduction

Optical fiber sensing (OFS) has been widely recognized as a promising and practical approach to perform distributed sensing and structural monitoring. Among various OFS techniques, Brillouin optical time domain analyzer (BOTDA) has recently drawn enormous research interests, owing to its long sensing range and robustness to noise. Conventional BOTDA transmits a high-power pulsed pump and a continuous wave (CW) single-frequency probe bi-directionally in the sensing fiber [1]. Interacting with the fiber acoustic waves, stimulated Brillouin scattering (SBS) transfers energy between the probe and the pump waves, which reaches the maximum when the probe-pump frequency gap is at the fiber's Brillouin frequency. As the Brillouin frequency is proportional to temperature and strain, the sensing of these parameters can be accomplished by detecting the Brillouin frequency shift (BFS) of the optical fiber.

Yet, transmitting a single frequency CW probe wave at each time, a frequency-scanning operation on the probe is necessary to construct the Brillouin gain spectrum (BGS) in conventional BOTDA, thus requiring multiple transmissions. In addition, for conventional Lorentzian curve fitting method, the BFS estimation accuracy is directly proportional to the signal-to-noise ratio (SNR) [2]. In order to enhance the SNR performance, thousands of measurements are taken for trace averaging. These two operations prolong the entire sensing process, usually in the time scale of minutes, making conventional BOTDA hardly meet the requirement of dynamic distributed sensing (DDS) [3]. In light of this, some modified BOTDA schemes have been proposed to avoid the frequency scanning process and improve the dynamicity of BOTDA, such as slope-assisted BOTDA [4–6], frequency-agile BOTDA [7,8] and frequency-comb BOTDA based on OFDM (OFDM-BOTDA) [9]. However, since SBS is polarization-dependent [10], a

#450977
Journal © 2022

https://doi.org/10.1364/OE.450977
Received 13 Dec 2021; revised 10 Feb 2022; accepted 11 Feb 2022; published 22 Feb 2022

polarization scrambler might be required to facilitate averaging [11], or a polarization maintaining fiber was required as the sensing medium [8]. Without a polarization scrambler or polarization maintaining fiber, the polarization dependence of temperature sensing could be suppressed by polarization division multiplexing according to [12]. In [13], a real single-shot BOTDA scheme was proposed, applying polarization division multiplexing on double-sideband (DSB) to deal with the polarization effect. However, it required a coherent receiver, which has complicated receiver structure, computation-heavy digital signal processing (DSP) and higher cost.

Fast and computation-efficient algorithms are necessary for the operation of dynamic BOTDA. In recent years, with the rapid development of machine learning (ML), some ML-based BFS extraction methods have been proposed to compete with the classic linear curve fitting (LCF) method [14–20], showing higher BFS estimation accuracy with extraordinary computation speed. In [16], the proposed back-propagation method improved frequency accuracy for 79.4% with only 1/12 elapsed time compared with LCF method. A convolutional neural network (CNN) based method was proposed in [21], to achieve a 0.5-meter spatial resolution with a 40-ns pump pulse. However, data samples with averaging operations were used in these models.

In this paper, we propose a dynamic polarization-insensitive BOTDA (D/PI-BOTDA) scheme over an optical direct-detection OFDM system. Polarization division multiplexing is implemented in the pump to resolve the SBS polarization dependence, while OFDM is utilized in the probe to avoid frequency scan and enable dynamic sensing. Besides, to address the real-time sensing requirement, we also propose a CNN-based BFS extraction network architecture and evaluate its performance over the proposed D/PI-BOTDA. The experimental results validated the polarization independence of the proposed scheme as well as its computation efficiency. A noteworthy suppression in Brillouin gain fluctuation was also observed. In addition, the BFS extraction process was accelerated by 10 times over the conventional LCF method.

2. Principles

2.1. Polarization-insensitive dynamic BOTDA

Figure 1 shows the principle of the proposed polarization-insensitive scheme. A double-sideband (DSB) OFDM signal is modulated to the probe, replacing the conventional continuous wave (CW), to generate an optical frequency comb as in Fig. 1(a). The baseband direct-detection OFDM signal $s_B(n)$ is expressed as [22–24]

$$\begin{aligned} s_B(n) &= \frac{1}{\sqrt{N}}\sum_{k=0}^{N-1} c_k e^{j2\pi\frac{k}{N}n} \\ c_k &= c_{N-k}, k = 1, 2, \ldots N-1 \\ c_k &= 0, k = 0, N/2 \end{aligned} \tag{1}$$

where N is the OFDM block size and c_k is the real payload at the k^{th} subcarrier. To create the intrinsic BFS, the baseband OFDM signal is firstly combined with a RF signal, and then modulated to the optical carrier, as

$$s_{RF}(n) = \frac{1}{\sqrt{N}}\sum_{k=0}^{N-1} c_k e^{j2\pi(f_{RF}+\frac{k}{N})n} \tag{2}$$

Replacing $\frac{k}{N}$ with f_k and taking the Fourier transform of (2) give the signal representation in the frequency domain as

$$s_{RF}(f) = \sum_{k=0}^{N-1} c_k\delta[2\pi(f - f_{RF} - f_k)] \tag{3}$$

where $\delta(\cdot)$ is the Dirac delta function and f_{RF} is the frequency of the RF signal. Thus, the transmitted optical OFDM signal with suppressed carrier is presented as

$$\begin{aligned} s(f) &= \sum_{k=0}^{N-1} c_k \delta[2\pi(f - f_c - f_{RF} - f_k)] + \sum_{k=0}^{N-1} c_k \delta[2\pi(f - f_c + f_{RF} - f_k)] \\ &= s_-(f) + s_+(f) \end{aligned} \tag{4}$$

where f_c is the frequency of the carrier. The high-frequency sideband $s_-(f)$, which contributes to SBS as Brillouin loss spectrum (BLS), is filtered out while only the Brillouin gain spectrum in the low-frequency sideband $s_+(f)$ remains, as in Fig. 1(b). The SBS occurring to the probe in orthogonal polarization can be formulated as

$$\tilde{s}_x(f) = H_x(f)s_+(f) \tag{5}$$

$$\tilde{s}_y(f) = H_y(f)s_+(f) \tag{6}$$

where $\tilde{s}_{x,y}(f)$ is the probe after SBS interaction in x, y polarizations and $H_{x,y}(f)$ is the complex Brillouin gain spectrum in (x, y) polarization, given by

$$H_{x,y}(f) = \exp[\frac{\eta_{x,y} g_0 \Delta v_B}{\Delta v_B + 2j(f - v_B)}] \tag{7}$$

in which $\eta_{x,y}$ is the mixing efficiency factor in x, y polarization respectively, g_0 is the Brillouin gain coefficient, Δv_B is the Brillouin spectrum linewidth and v_B is the BFS. According to [10], the mixing efficiency factor between the two counter-propagating waves can be formulated as

$$\eta_{x,y} = \frac{1}{2}(1 + s_{1px,y}s_{1s} + s_{2px,y}s_{2s} - s_{3px,y}s_{3s}) \tag{8}$$

where $s_{px,y} = (s_{1px,y}, s_{2px,y}, s_{3px,y})$ and $s_s = (s_{1s}, s_{2s}, s_{3s})$ are the normalized Stokes vectors for (x, y) polarization pump and probe, respectively. When the OFDM probe meets the orthogonal-polarized pump with a random state of polarization (SOP) as shown in Fig. 1(c), we have

$$s_{px} + s_{py} = (s_{1px} + s_{1py}, s_{2px} + s_{2py}, s_{3px} + s_{3py}) = 0 \tag{9}$$

$$s_s = (s_{1s}, s_{2s}, s_{3s}) = (\cos 2\psi \cos 2\chi, \sin 2\psi \cos 2\chi, \sin 2\chi) \tag{10}$$

where ψ and χ are the Poincaré sphere parameters. From Eqs. (8) to (10), we can easily derive

$$\eta_x + \eta_y = 1 \tag{11}$$

According to [11], $|H_{x,y}(f)|$ can be obtained by channel estimation, as

$$|H_{x,y}(f)| = |\frac{\tilde{s}_{x,y}(f)}{s_+(f)}| = \frac{2\eta_{x,y} g_0 \Delta v_B{}^2}{\Delta v_B{}^2 + 4(f - v_B)^2} \tag{12}$$

In fact, the total Brillouin gain profile $G(f)$ is the summation of the orthogonal polarization after the photodiode (PD), which can be expressed as:

$$G(f) = \frac{2g_0 \Delta v_B{}^2}{\Delta v_B{}^2 + 4(f - v_B)^2} \tag{13}$$

Equation (13) indicates the direct-detected Brillouin gain is insensitive to the polarization effect.

Optics EXPRESS

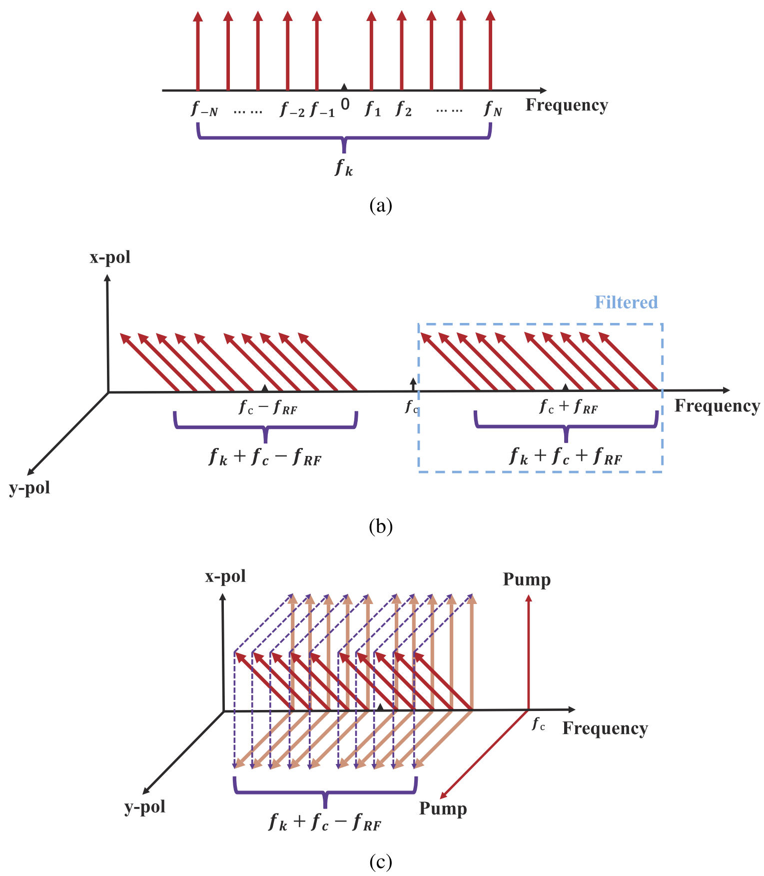

Fig. 1. Principle of single-shot direct-detection BOTDA. (a) Baseband OFDM optical frequency comb; (b) Single-sideband OFDM probe with lower sideband only; (c) Projection of OFDM probe to dual-polarized pump with SBS interaction.

2.2. CNN-based BFS extraction approach

To evaluate the performance of CNN-based network architectures on BFS estimation, three networks, conventional CNN, BRNet and BR2Net, are implemented in our experiment, shown in Fig. 2. Basically, BFS is a location information corresponding to the frequency range. However, the location information is invisible to the convolution kernels. Therefore, a linear ascending series $\{1, 2, \ldots\}$ is inserted along the input frequency as the second channel to involve the location information, serving as the positional encoding in [25]. Fig. 2(a) shows the data input after being normalized by an instance-normalization (IN) layer [26], which carries out the normalization within each data without affecting the batch and the channel dimension. The data input is reshaped from $500 \times 2 \times 127$ to $100 \times 2 \times 5 \times 127$ to enable the 2D convolution, where 500 is the batch size, 2 as mentioned is the channel number and 127 is the number of frequency contained in one BGS. The CNN model shown in Fig. 2(b) consists of four 2D convolution layers and one max-pooling layer. Each convolution layer is followed by a rectified linear unit (ReLu) activation function and a batch-normalization (BN) layer [27]. It should be noted that BFS estimation is intrinsically a regression problem, and our experiments show that it is difficult for the network to predict the frequency output accurately. Thus, one classification head and one regression head are utilized in the network. The output frequency range is divided into 127 segments and the classification head is used to predict the segment with BFS. Meanwhile the regression head estimates the BFS location within the predicted segment. This configuration is preserved throughout all the architectures in this paper.

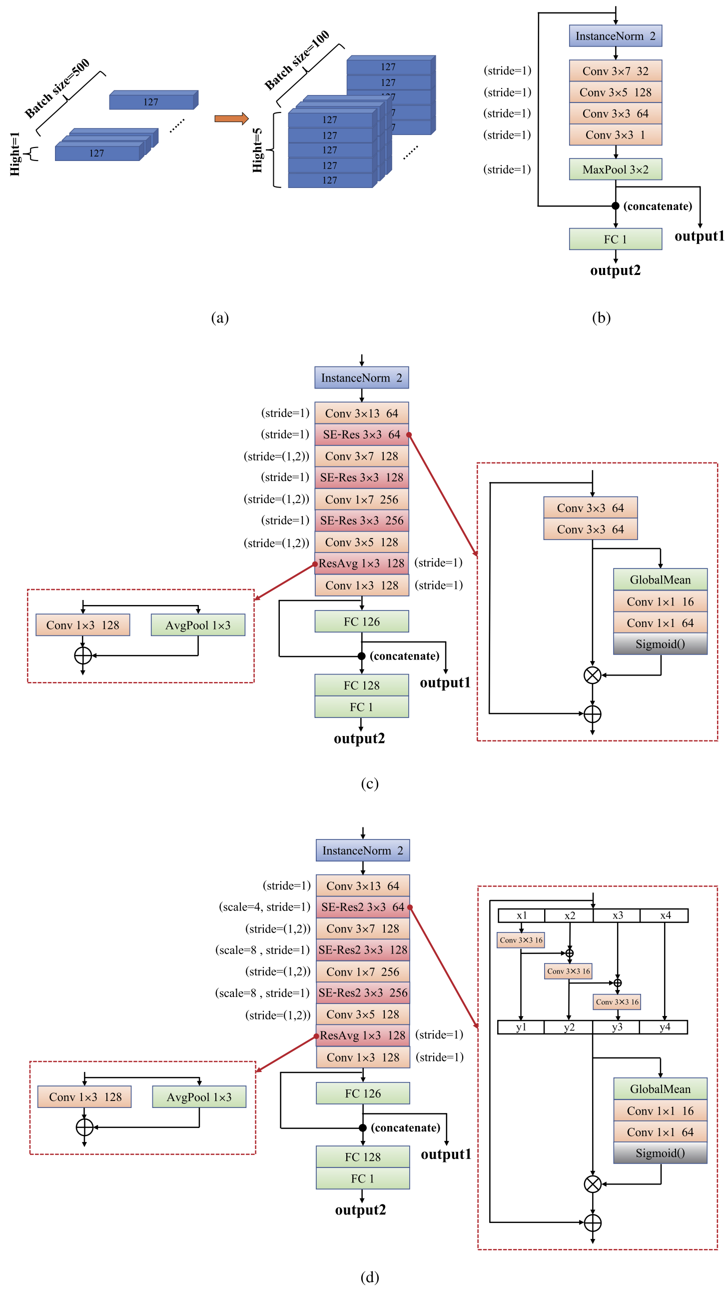

Fig. 2. (a) Input data dimension reshaping; (b) conventional four-layer CNN; (c) proposed BRNet; (d) proposed BR2Net.

In Fig. 2(c), SE-ResNet blocks [28] are added in the network, named BRNet. One SE-ResNet block consists of two convolution layers and a Squeeze-and-Excitation (SE) module. The global information of the feature is captured by a global average pooling layer in SE and the attention weights are learnt by later convolution layers. The SE module enhances the important channels by assigning large weights and excites the input by applying a channel-wise multiplication, represented by ⊗. While the input of the SE-ResNet block is directly connected to the block output by element-wise addition, which is denoted by ⊕. This residual connection aims to deal with the gradient vanishing problem by preserving the residual information [29]. Three SE-ResNet blocks are implemented in total and each is followed by a convolution layer to match the input channel number for next block. After these cascaded blocks, an average pooling layer is induced, the output of which is added to the output of the following convolution layer. In Fig. 2(d), BR2Net is proposed by embedding SE-Res2Net blocks [30] in the architecture. In the structure of Res2Net, the feature is equally divided into several groups along the channel dimension, and the group number is put forward as a new dimension for convolution, named *scale*. The convolution output from the previous group is added with the current group and fed into the current convolution layer. All group outputs are concatenated together as the final output and processed by a SE module. There are three SE-Res2Net blocks in the network with $scale = 4\ or\ 8$. The application of SE-Res2Net block enriches the diversity of receptive fields, which helps to extract both local and global features with a relatively smaller number of training parameters.

3. Experimental setup and data sampling

Figure 3 depicts the full picture of the experimental setup. An external cavity laser (ECL) operating at 1550 nm with a linewidth of 100 kHz was used as the optical carrier. The laser output was split into two branches. For the upper branch, an OFDM signal with block size of 256 was generated by an arbitrary waveform generator (AWG) with a sampling rate of 1.28 GSa/s. Only 127 subcarriers were loaded with data while the others were loaded with the Hermitian conjugate, for the real-valued data intensity modulation and direct detection (IM/DD). Before being fed to the intensity modulator, the OFDM signal was firstly up-converted by mixing with an 11 GHz RF clock signal, generated by an analog signal generator (ASG). This sinusoidal signal was chosen such that the baseband OFDM signal was upconverted to an intermediate frequency of 11 GHz, to cover the BGS. After up-conversion, the electrical signals ranged from 10.36 GHz to 11.64 GHz. The channel amplitude response of the subcarriers within this frequency range reflected the BGS as denoted in (12), and as in [11]. An erbium-doped fiber amplifier (EDFA) was used to boost the power of the probe signal to around −10 dBm and an optical isolator was placed before the FUT to block the reflection. For the lower branch, the pump was modulated with a pulse with a repetition rate of 100 kHz and a pulse width of 100 ns by a high extinction ratio (ER) modulator (>30 dB). It should be noted that the pump pulse width used here is not the optimal configuration and a better SNR performance can be achieved for a longer pump pulse width [31]. However, the pump pulse width is needed to be no longer than the OFDM frame length, that is, 200 ns in the time domain. The peak power of the pump pulse was amplified to 20 dBm by an EDFA. A beam splitter (BS) was used to form the dual-polarization pump, with one arm delayed for 20 meters, a pulse width length, to avoid beating. After recombined by a polarization beam combiner (PBC), the polarization-multiplexing pump was fed into the FUT to interact with the probe. The length of the FUT was 900 m, and a water bath was placed at the far end of the FUT with a heating length of 40 m. The temperature was set from 25°C to 65°C with a step of 10°C. The OFDM subcarriers were spaced by 5 MHz, translating to a spatial resolution of 20 m. An optical circulator was used after the water bath to direct the probe to the receiver. After passing through a band-pass filter (BPF) to filter out the high-frequency sideband, the probe was fed into a PD before being captured by an oscilloscope. The signal-to-signal beating interference (SSBI) fell around DC, while the target BGS was around the carrier frequency at 11 GHz to stay free from SSBI. Offline digital signal processing (DSP) was then performed to reconstruct the BGS. After down-sampling and synchronization, the received signal was divided

Optics EXPRESS

into cascaded OFDM segments and fast Fourier Transform (FFT) was conducted to compute the complex value of each subcarrier. Same as [11], the first several segments without SBS effect were used for channel estimation to compensate the channel response, and the rest symbols were the payload for BFS estimation.

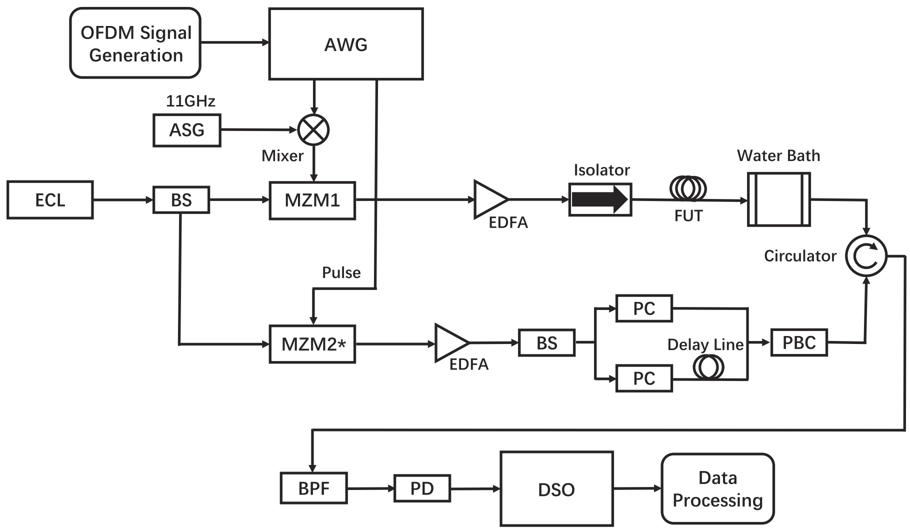

Fig. 3. Experiment setup. ECL: external cavity laser, BS: beam splitter, AWG: arbitrary waveform generator, ASG: analog signal generator, MZM: Mach–Zehnder modulator(* means high extinction ratio), EDFA: Erbium-doped fiber amplifier, FUT: Fiber Under Test, PC: polarization controller, PBC: polarization beam combiner, BPF: band-pass filter, PD: photodetector, DSO: digital storage oscilloscope.

For the training data set, we generated simulated BGS using the Lorentzian model [18] ranging from 10.365 GHz to 10.995 GHz with a step of 5 MHz. The BFS was set from 10.400 GHz to 10.8999 GHz with a step of 0.1 MHz and the Brillouin linewidth was set from 20 MHz to 59 MHz with a step of 1 MHz. Further, for the ergodicity of the system over possible signal to noise ratio (SNR), we induced additive white Gaussian noise (AWGN) to BGS generation by setting the SNR equal to 12 dB, 14 dB, 16 dB, 18 dB and 20 dB. Thus, the sample size of the training data set was $600 \times 40 \times 5 = 120000$. For each input data, the dimension was 127 corresponding to the number of frequencies contained in the BGS. The range of the spectrum was normalized to 1, so that the corresponding BFS was re-calculated as following equation according to [19]:

$$BFS_n = \frac{BFS - f_{min}}{f_{max} - f_{min}} \tag{14}$$

where f_{min}/f_{max} is the minimum/maximum frequency collected in BGS respectively.

The outputs from the classification head and the regression head in the model were used to calculate a cross-entropy loss and a $L2$ loss respectively. The model was trained by Adam optimizer [32] for 20 epochs to depress the sum of the cross-entropy and $L2$ loss. The learning rate was initialized as 0.001 and decayed by ratio=0.1 for every 8 epochs.

4. Results and discussion

First, we test the sensing performance of the proposed D/PI-BOTDA. It should be noted that all data is collected by one-shot measurement. Figure 4(a) shows the obtained BGS under the temperature of 65°C with the curve fitting results in the inset, giving an estimation BFS of

Optics EXPRESS

10.8905 GHz. Figure 4(b) presents the corresponding reconstructed Brillouin spectrogram. The Brillouin gain of each FUT position has been normalized within the range of [0,1] and the sudden change of BFS is easily observed at heated part of the FUT. Figure 4(c) estimates the distributed BFS along the FUT under different temperatures of the water bath. The whole 940-meter FUT is divided into 47 segments due to the 20-meter spatial resolution. The non-uniform BFS distribution within the 40-meter heated FUT is attributed to the BGS crosstalk between the last unheated FUT segment and the first heated FUT segment, due to misalignment of the probe and the pump. Whereas, the 40-m FUT has at least one complete data frame, which we takes as the real estimated BFS for the rest of the paper. Figure 4(d) depicts how the BFS of the heated FUT rises as the temperature increases. The measured BFS, as a function of temperature, determines a linear correlation coefficient of 0.9935. The measured temperature sensitivity is around 1.2 MHz/°C. The relatively larger curve fitting deviation at temperature 25°C and 45°C wi mainly caused by the insufficient SNR, owing to the single-shot measurement.

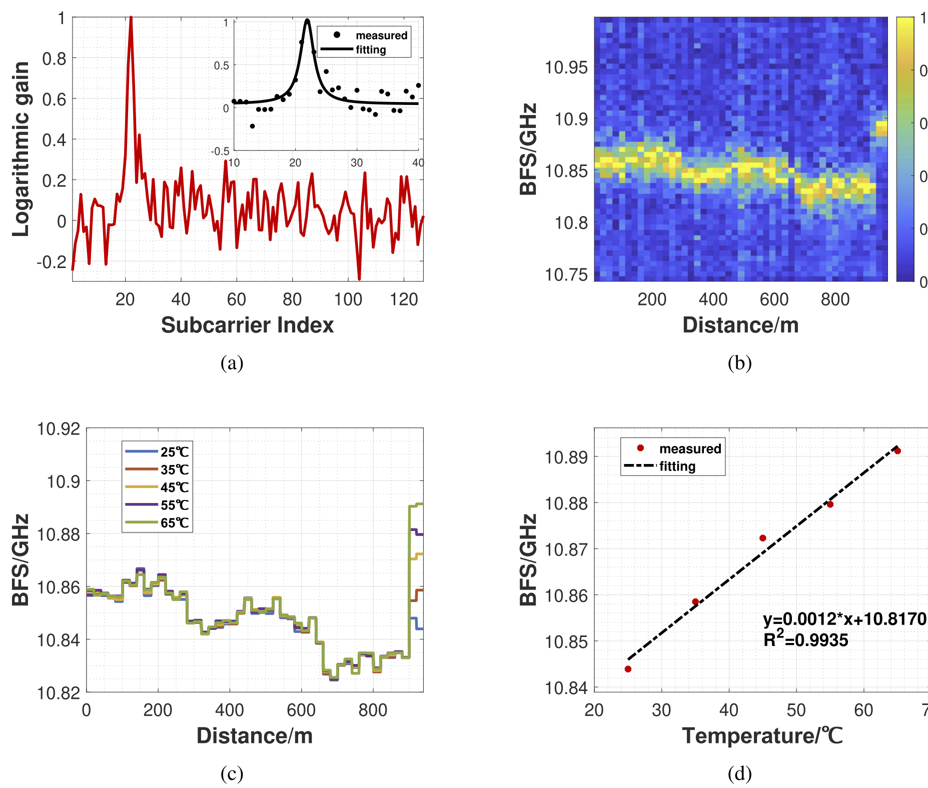

Fig. 4. (a) Reconstructed BGS under the temperature of 65°C with single-shot measured data, Inlet is the data for LCF to estimate BFS; (b) Reconstructed Brillouin spectrogram with a 65°C water bath; (c) BFS distribution under different heating temperature along the FUT; (d) BFS over temperature changes as a function. The black line is the linear curve fitting result.

Next, to validate the proposed polarization-insensitive scheme, we add a polarization controller (PC) to change the state of polarization (SOP) of the OFDM probe before it is launched into the FUT. Figure 5 shows the measured Brillouin gain distribution when the SOP is randomly changed by 100 times and all data has been normalized. The x-axis indicates the deviation of the measured Brillouin gain from the average value while the y-axis is the probability of following into the deviation. Both x and y are dimensionless. The pulse width is set as 100 ns for each

Optics EXPRESS

polarization in both schemes to keep the maximum Brillouin gain the same. In Fig. 5(a), the Brillouin gain is severely influenced by the relative SOP change between the probe and the pump, presenting almost a uniform distribution with a variance of 1.514×10^{-3}. Figure 5(b) shows that the Brillouin gain variation is significantly squeezed by around 4.38 times in our proposed dual-polarization scheme, with a variance of 3.456×10^{-4}. This result indicates that our proposed scheme has satisfactory resistance to the SBS polarization dependence.

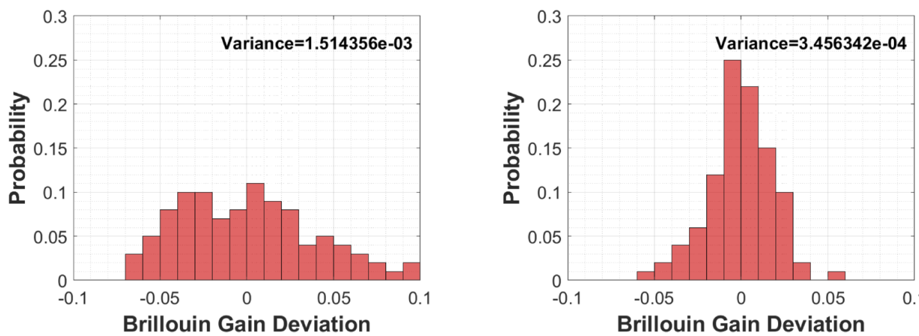

(a) (b)

Fig. 5. Brillouin gain distribution for 100 measurements (a) with single-polarization scheme; (b) with proposed dual-polarization scheme.

Finally, we perform evaluation to the CNN-based BFS extraction method which is proposed against low SNR condition. The dataset contains 500 samples for each temperature from 25°C to 65°C with a step of 10°C, totally 2500 samples, and the calculated root-mean-square-error (RMSE) of the estimated BFS serves as the evaluation benchmark. Figure 6(a) shows the performance of the conventional LCF, cross correlation-based method (XCM) [33], CNN, and the proposed BRNet and BR2Net. As shown, the conventional CNN method only outperforms the LCF under 35°C and 45°C, yet showing worse accuracy on the others. The variation of the XCM is generally worse than LCF except at 35°C. This degradation is due to the large frequency step of BGS [14]. Both the proposed BRNet and BR2Net show higher accuracy than the LCF at 25°C, 35°C, and 45°C, and similar performance at 55°C and 65°C. Since Brillouin gain is proportional to the temperature change [34], the results match the conclusion of [19], where CNN-based BFS extraction methods performed better than the LCF under the condition of low SNR. To investigate the influence of the number of the SE-ResNet blocks on the performance, we also examine the performance of the BRNet implemented with three/six SE-ResNet blocks, respectively. Figure 6(b) illustrates that more SE-ResNet blocks hardly improve the estimation accuracy of the whole network. Hence, the three-block profile is preserved in the following analysis. From the experimental results in Fig. 6(a) and 6(b), we can see that the BRNet and the BR2Net show similar performance, while the total number of training parameters required in the three SE-Res2Net blocks of BR2Net is only 87936, which is 16.6 times less than that in SE-ResNet blocks. Table 1 shows the BFS extraction time of mentioned methods for 2500 samples. The XCM, the one with the least computational complexity, takes the shortest time. Overall, the CNN-based methods are much more time-efficient compared with the conventional LCF method and specifically, the BR2Net is 90.27% faster than LCF method and 11.34% faster than the BRNet. These prove the computation efficiency of the proposed BR2Net.

Table 1. BFS extraction time of 2500 samples.

Method	LCF	XCM	CNN	BRNet	BR2Net
Time/s	26.52	0.11	1.91	2.91	2.58

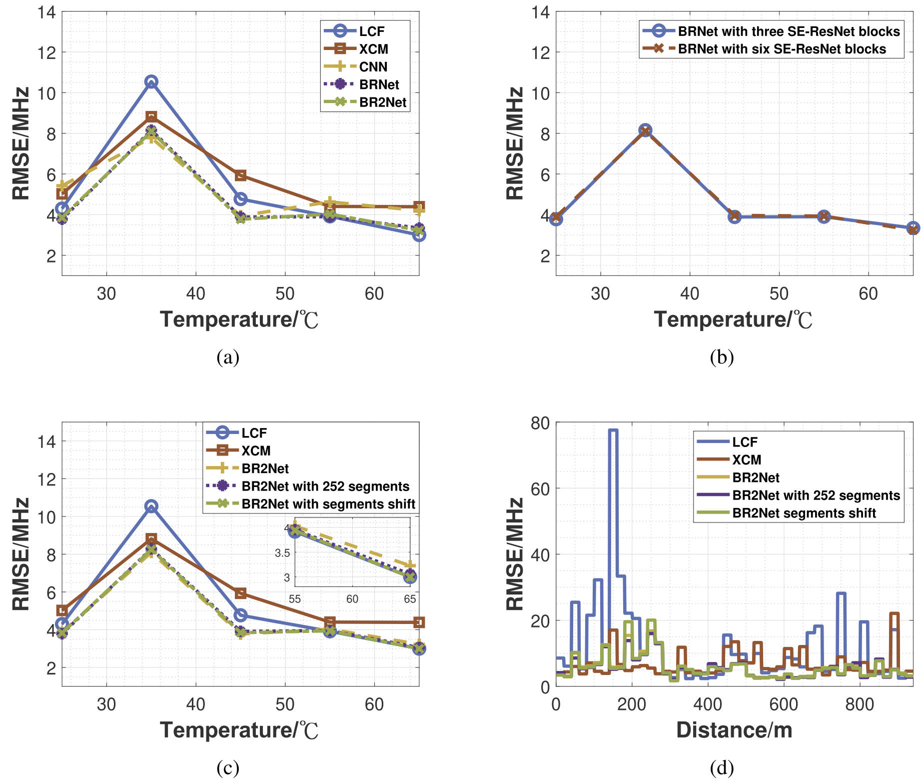

Fig. 6. (a) Estimated BFS RMSE comparison of different BFS extraction methods under different temperatures; (b) estimated BFS RMSE comparison between proposed architecture with three and six SE-ResNet blocks under different temperatures; (c) estimated BFS RMSE comparison of three variations of proposed architecture with SE-Res2Net under different temperatures; (d) distributed estimated BFS RMSE comparison between proposed architecture with SE-Res2Net blocks and conventional LCF method.

During the training, we find the application of the sigmoid function limits the estimation accuracy when the target BFS is located at the segment edge, due to the open interval property of its output ((0,1)). As a response, we implement two variations of the BR2Net. In the first variation, we extend the original 126 segments to 252 segments for strengthening the influence of the classification results while weakening that of the regression. Inspired by avoiding sigmoid outputting the boundary value in ML, in the second variation, we implement a second target segment-BFS pair which is generated by shifting the original one to the left for half-segment length. In this way, the edge of original segments becomes the middle point of the new segment and vice versa. The network learns from both segment-BFS pairs and picks the regression result with a relatively smaller absolute input value to the sigmoid as the final estimated BFS. Figure 6(c) shows the performance comparison of the BR2Net variations, where the inset is the partially enlarged sketch of the 65°C case. The proposed two variations show similar performance from 25°C to 55°C, and both outperform the LCF and the BR2Net at 65°C. Specifically, the segment-shift method beats the 252-segment one, achieving a competitive RMSE with the LCF method. Figure 6(d) depicts the distributed RMSE performances among the LCF, the XCM and the proposed BR2Net under 65°C water bath, verifying that the BR2Net can achieve a relatively smaller distributed RMSE compared with LCF and XCM, especially at the near end of the FUT where the SNR is low, which illustrates a higher stability of the proposed architecture.

5. Conclusion

We have proposed a dynamic polarization-insensitive BOTDA. The OFDM-based probe enables a single-shot measurement to acquire the Brillouin gain spectrum, while the polarization-multiplexing pump removes the Brillouin gain uncertainty caused by the polarization dependence of SBS. We have conducted distributed temperature sensing experiments, showing that our proposed scheme can achieve an impressive Brillouin gain fluctuation suppression by 4.38 times compared to the case without polarization diversity, with a temperature sensing coefficient of 1.2 MHz/°C. Furthermore, to improve the BFS estimation accuracy, we have implemented a 2D CNN-based BFS extraction architecture, the BR2Net. The results have indicated the proposed model can outperform the conventional LCF method, with an extra benefit of speeding up the extraction process over 10 times.

Disclosures. The authors declare no conflicts of interest.

Data availability. Data underlying the results presented in this paper are not publicly available at this time but may be obtained from the authors upon reasonable request.

References

1. T. Horiguchi, K. Shimizu, T. Kurashima, M. Tateda, and Y. Koyamada, "Development of a distributed sensing technique using Brillouin scattering," J. Lightwave Technol. **13**(7), 1296–1302 (1995).
2. M. A. Soto and L. Thévenaz, "Modeling and evaluating the performance of Brillouin distributed optical fiber sensors," Opt. Express **21**(25), 31347–31366 (2013).
3. K. Hotate and S. S. L. Ong, "Distributed dynamic strain measurement using a correlation-based Brillouin sensing system," IEEE Photonics Technol. Lett. **15**(2), 272–274 (2003).
4. R. Bernini, A. Minardo, and L. Zeni, "Dynamic strain measurement in optical fibers by stimulated Brillouin scattering," Opt. Lett. **34**(17), 2613–2615 (2009).
5. Y. Peled, A. Motil, L. Yaron, and M. Tur, "Slope-assisted fast distributed sensing in optical fibers with arbitrary Brillouin profile," Opt. Express **19**(21), 19845–19854 (2011).
6. D. Ba, B. Wang, D. Zhou, M. Yin, Y. Dong, H. Li, Z. Lu, and Z. Fan, "Distributed measurement of dynamic strain based on multi-slope assisted fast BOTDA," Opt. Express **24**(9), 9781–9793 (2016).
7. Y. Peled, A. Motil, and M. Tur, "Fast Brillouin optical time domain analysis for dynamic sensing," Opt. Express **20**(8), 8584–8591 (2012).
8. D. Zhou, Y. Dong, B. Wang, C. Pang, D. Ba, H. Zhang, Z. Lu, H. Li, and X. Bao, "Single-shot BOTDA based on an optical chirp chain probe wave for distributed ultrafast measurement," Light: Sci. Appl. **7**(1), 32 (2018).
9. C. Jin, N. Guo, Y. Feng, L. Wang, H. Liang, J. Li, Z. Li, C. Yu, and C. Lu, "Scanning-free BOTDA based on ultra-fine digital optical frequency comb," Opt. Express **23**(4), 5277–5284 (2015).
10. M. O. van Deventer and A. J. Boot, "Polarization properties of stimulated Brillouin scattering in single-mode fibers," J. Lightwave Technol. **12**(4), 585–590 (1994).
11. C. Zhao, M. Tang, L. Wang, H. Wu, Z. Zhao, Y. Dang, J. Wu, S. Fu, D. Liu, and P. P. Shum, "BOTDA using channel estimation with direct-detection optical OFDM technique," Opt. Express **25**(11), 12698–12709 (2017).
12. J. Yang, C. Yu, Z. Chen, J. Ng, and X. Yang, "Suppression of polarization sensitivity in BOTDA fiber distributed sensing system," in *Proceedings Volume 7004, 19th International Conference on Optical Fibre Sensors*, (IEEE, 2008), pp. 607–611.
13. J. Fang, P. Xu, Y. Dong, and W. Shieh, "Single-shot distributed Brillouin optical time domain analyzer," Opt. Express **25**(13), 15188–15198 (2017).
14. A. K. Azad, L. Wang, N. Guo, H.-Y. Tam, and C. Lu, "Signal processing using artificial neural network for BOTDA sensor system," Opt. Express **24**(6), 6769–6782 (2016).
15. B. Wang, L. Wang, N. Guo, Z. Zhao, C. Yu, and C. Lu, "Deep neural networks assisted BOTDA for simultaneous temperature and strain measurement with enhanced accuracy," Opt. Express **27**(3), 2530–2543 (2019).
16. Z. Cao, N. Guo, M. Li, K. Yu, and K. Gao, "Back propagation neutral network based signal acquisition for Brillouin distributed optical fiber sensors," Opt. Express **27**(4), 4549–4561 (2019).
17. S. Liehr, L. A. Jäger, C. Karapanagiotis, S. Münzenberger, and S. Kowarik, "Real-time dynamic strain sensing in optical fibers using artificial neural networks," Opt. Express **27**(5), 7405–7425 (2019).
18. B. Wang, N. Guo, L. Wang, C. Yu, and C. Lu, "Robust and fast temperature extraction for Brillouin optical time-domain analyzer by using denoising autoencoder-based deep neural networks," IEEE Sens. J. **20**(7), 3614–3620 (2020).
19. Y. Chang, H. Wu, C. Zhao, L. Shen, S. Fu, and M. Tang, "Distributed Brillouin frequency shift extraction via a convolutional neural network," Photonics Res. **8**(5), 690–697 (2020).
20. C. Karapanagiotis, A. Wosniok, K. Hicke, and K. Krebber, "Time-efficient convolutional neural network-assisted Brillouin optical frequency domain analysis," Sensors **21**(8), 2724–2733 (2021).

21. Z. Ge, L. Shen, H. Wu, Z. Zhao, and M. Tang, "Spatial resolution improvement of a long pulse BOTDA sensor using a convolutional neural network," in *Optoelectronics and Communications Conference (OECC)*, (2021).
22. B. J. C. Schmidt, A. J. Lowery, and J. Armstrong, "Experimental demonstrations of electronic dispersion compensation for long-haul transmission using direct-detection optical OFDM," J. Lightwave Technol. **26**(1), 196–203 (2008).
23. J. Armstrong, "OFDM for optical communications," J. Lightwave Technol. **27**(3), 189–204 (2009).
24. S. D. Dissanayake and J. Armstrong, "Comparison of ACO-OFDM, DCO-OFDM and ADO-OFDM in IM/DD systems," J. Lightwave Technol. **31**(7), 1063–1072 (2013).
25. A. Vaswani, N. Shazeer, N. Parmar, J. Uszkoreit, L. Jones, A. N. Gomez, Ł. Kaiser, and I. Polosukhin, "Attention is all you need," in *Advances in neural information processing systems*, (2017), pp. 5998–6008.
26. D. Ulyanov, A. Vedaldi, and V. Lempitsky, "Instance normalization: The missing ingredient for fast stylization," arXiv preprint arXiv:1607.08022 (2016).
27. S. Ioffe and C. Szegedy, "Batch normalization: Accelerating deep network training by reducing internal covariate shift," in *International conference on machine learning*, (PMLR, 2015), pp. 448–456.
28. J. Hu, L. Shen, and G. Sun, "Squeeze-and-excitation networks," in *Proceedings of the IEEE conference on computer vision and pattern recognition*, (2018), pp. 7132–7141.
29. K. He, X. Zhang, S. Ren, and J. Sun, "Deep residual learning for image recognition," in *Proceedings of the IEEE conference on computer vision and pattern recognition*, (2016), pp. 770–778.
30. S. Gao, M.-M. Cheng, K. Zhao, X.-Y. Zhang, M.-H. Yang, and P. H. Torr, "Res2net: A new multi-scale backbone architecture," IEEE transactions on pattern analysis and machine intelligence (2019).
31. J. Smith, A. Brown, M. DeMerchant, and X. Bao, "Pulse width dependance of the Brillouin loss spectrum," Opt. Commun. **168**(5-6), 393–398 (1999).
32. D. P. Kingma and J. Ba, "Adam: A method for stochastic optimization," arXiv preprint arXiv:1412.6980 (2014).
33. M. A. Farahani, E. Castillo-Guerra, and B. G. Colpitts, "Accurate estimation of brillouin frequency shift in Brillouin optical time domain analysis sensors using cross correlation," Opt. Lett. **36**(21), 4275–4277 (2011).
34. T. R. Parker, M. Farhadiroushan, V. A. Handerek, and A. J. Rogers, "Temperature and strain dependence of the power level and frequency of spontaneous Brillouin scattering in optical fibers," Opt. Lett. **22**(11), 787–789 (1997).